

iPAT: Applications for fast and cardiovascular MR imaging

Dietrich O¹, Nikolaou K¹, Wintersperger BJ¹, Flatz W¹, Nittka M², Petsch R², Kiefer B², Schoenberg SO¹.

¹ Department of Clinical Radiology, University of Munich, Klinikum Großhadern, Munich, Germany

² Siemens AG, Medical Solutions, Erlangen, Deutschland

ELECTRONIC PREPRINT VERSION:

Not for commercial sale or for any systematic external distribution by a third party

Final version: *electromedica* 2002; **70**(2): 133–146

Abstract

Parallel imaging is a new magnetic resonance imaging method based on the parallel use of more than one receiver coil to acquire image data with less phase-encoding steps than in conventional imaging. Advantages of parallel acquisitions techniques are acceleration of imaging, reduction of motion artifacts, and decrease of susceptibility sensitivity. In this article, the basic reconstruction techniques SMASH and SENSE are described, and clinical applications of parallel acquisition techniques are demonstrated for functional cardiac imaging, pulmonary angiography and perfusion imaging, renal angiography, and high-resolution larynx imaging.

Keywords:

Integrated parallel acquisition techniques; Parallel imaging; Cardiovascular imaging.

Corresponding author:

Dr. Olaf Dietrich

Klinikum der Universität München
Institut für Klinische Radiologie
Marchioninistraße 15
D-81377 München
Deutschland
Tel. +49 (0)89 7095-3623
Fax. +49 (0)89 7095-4627
E-Mail: od@dtrx.de

Basic principles

In the last years, a number of new magnetic resonance imaging (MRI) methods were developed and quickly accepted by researchers and manufacturers which are now known as parallel acquisition techniques (PAT), partially parallel acquisition (PPA), or (partially) parallel imaging. The initial motivation for these techniques was the acceleration of image acquisition by decreasing the number of (phase-encoding) imaging steps without reducing the image resolution. The basic principle of these new methods is to acquire image data simultaneously by two or more receiver coils with different spatial sensitivity profiles. During image reconstruction, information that is usually acquired consecutively (and thus time-consuming) by phase-encoding steps can then be substituted by data determined from the complementary information of the different receiver channels.

Main applications of PAT are the reduction of examination time by faster imaging, the increase of spatial resolution in a given acquisition time, e.g., for breath-hold examinations, and the increase of temporal resolution in dynamic imaging. Further applications of PAT besides the acceleration of image acquisition are the reduction of artifacts by shortening the echo train length in single shot sequences [1] and the improvement of data integrity by using redundant image information as navigator echoes for motion correction [2]. Imaging moving organs or tissues can also be improved by averaging repeated PAT acquisitions with shorter individual imaging times compared to a single longer acquisition.

As mentioned above, a typical application of PAT is the reduction of the number of acquired lines in the frequency domain to shorten the acquisition time. E.g., by acquiring only every second or third line, imaging can be accelerated by an “acceleration factor” R of 2 or 3, respectively. However, by decreasing the sampling density in the phase-encoding direction the field of view (FOV) is reduced in this direction as well while the spatial image resolution, i.e., the pixel size, remains constant. Thus, folding artifacts occur caused by imaging objects larger than this reduced FOV (Fig. 1) and special reconstruction methods are required to remove these artifacts.

Several techniques have been suggested for the PAT image reconstruction from reduced data sets which can be divided into two groups: techniques working on the data in frequency domain (k-space) and techniques working on the Fourier transformed data in the image domain. To the former techniques belong SMASH (simultaneous acquisition of spatial harmonics) [3], AUTO-SMASH (auto-calibrating SMASH) [4], and GRAPPA (generalized auto-calibrating partially parallel acquisition) [5]. The most

important techniques working in image space are SENSE MRI (sensitivity-encoded MRI) [6], PILS (parallel imaging with localized sensitivities) [7], and SPACE RIP (sensitivity profiles from an array of coils for encoding and reconstruction in parallel) [8].

All these methods require some information about the spatial sensitivity profiles of the different receiver coils. This information can be acquired either in an additional scan prior to the PAT scan or integrated as few additional phase-encoding steps within the PAT scan.

Reconstruction in the frequency domain

The basic principle of the SMASH approach and newer similar techniques is to add missing data lines in k-space before the actual image reconstruction by Fourier transformation is performed. Missing lines are calculated from acquired neighboring lines using the additional information that is provided by the coil sensitivity profiles. The original SMASH reconstruction is based on applying sinusoidal spatial coil sensitivity profiles to calculate those lines in k-space that were not acquired [3].

In the general case, the MR signal $S(k_x, k_y)$ in k-space of a two-dimensional slice with proton density $\rho(x, y)$ can be written as

$$\begin{aligned} S(k_x, k_y) &= \iint dx dy C(x, y) \rho(x, y) \exp(-ik_x x - ik_y y) \\ &= F[\rho](k_x, k_y) \end{aligned} \quad (1)$$

with the spatial coil sensitivity $C(x, y)$; $F[\rho]$ denotes the Fourier transform of the spin density $\rho(x, y)$. The ideal case for conventional imaging is constant coil sensitivity, i.e., $C_0(x, y) = 1$, corresponding to a homogeneous intensity distribution over the acquired FOV.

For the SMASH technique, the receiver coil elements are operated individually such that their sensitivity profiles and subsequently their signals can be linearly combined during the reconstruction process as shown in (Fig. 2). Having an array of receiver coils with different sensitivity profiles $C^j(x, y)$, image reconstruction can be described as

$$\begin{aligned} S(k_x, k_y) &= \iint dx dy [\sum_j n^j C^j(x, y)] \\ &\quad \rho(x, y) \exp(-ik_x x - ik_y y) \end{aligned} \quad (2a)$$

$$= \sum_j n^j [\iint dx dy C^j(x, y) \rho(x, y) \exp(-ik_x x - ik_y y)] \quad (2b)$$

$$= \sum_j n^j S^j(k_x, k_y) \quad (2c)$$

with coefficients n^j that describe a superposition of coil sensitivities and of the signals $S^j(k_x, k_y)$ of the individual coils.

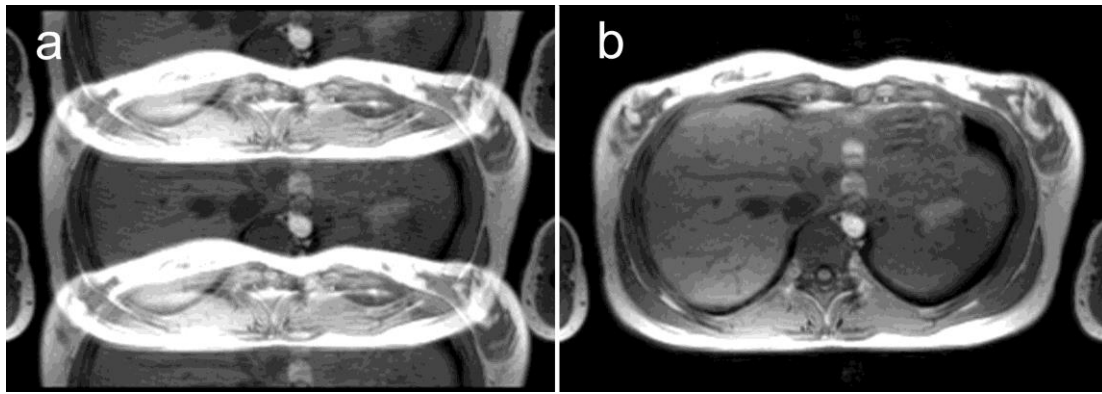


Figure 1. Conventional and PAT image reconstruction: (a) Folding artifacts in PAT image with reduced number of phase-encoding lines (acceleration factor $R=2$ in anterior–posterior direction). Instead of displaying the reduced FOV, the full FOV with duplicated image information is shown. (b) Image after PAT reconstruction; the artifacts are removed.

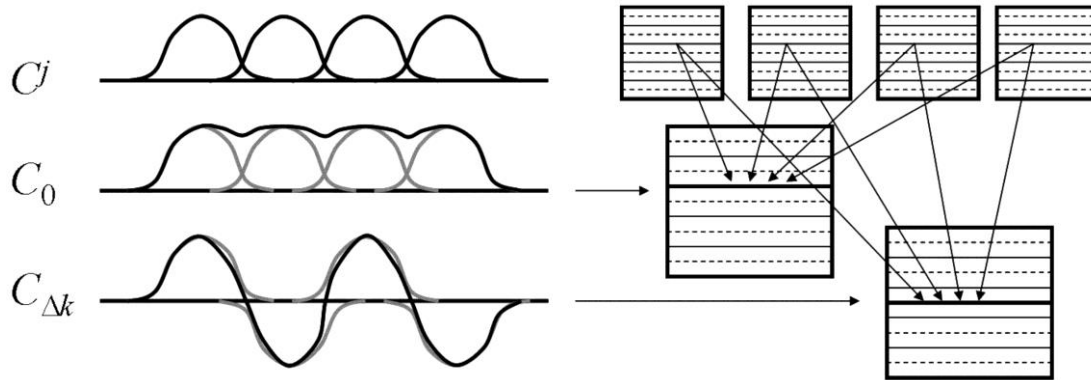


Figure 2. SMASH reconstruction: Spatial sensitivity profiles C^j of single coil elements, superposition C_0 yielding an approximately constant profile, and superposition $C_{\Delta k}$ yielding an approximately sinusoidal profile. C_0 is used to reconstruct the acquired k-space lines (solid lines) from data of the single coils; $C_{\Delta k}$ is used to reconstruct those lines that were not originally acquired (dashed lines).

By choosing appropriate weighting coefficients n^j , the combination of the coil elements may either yield the constant spatial coil profile $C_0(x, y)$ or a sinusoidal coil profile with a low spatial frequency Δk_y . The latter sensitivity profile can be written as complex coil profile

$$C_{\Delta k}(x, y) = \cos(\Delta k_y y) + i \sin(\Delta k_y y) = \exp(i\Delta k_y y). \quad (3)$$

To obtain these profiles, the spatial configuration and the individual sensitivity profiles $C^j(x, y)$ of the coil elements must be suited to yield both constant and sinusoidal net sensitivities in an appropriate superposition. That means, the different coil sensitivities C_0 and $C_{\Delta k}$ must be representable as linear combinations

$$C_0(x, y) = \sum_j n_0^j C^j(x, y) = 1 \quad (4a)$$

$$C_{\Delta k}(x, y) = \sum_j n_{\Delta k}^j C^j(x, y) = \exp(i\Delta k_y y) \quad (4b)$$

where the coefficients $n_0^j, n_{\Delta k}^j$ are to be determined such that the desired net sensitivity is achieved. To calculate these coefficients, the separate coil sensitivity maps

$C^j(x, y)$ must be known, e.g., from measurements in a pre-scan.

Calculating k-space lines with the constant sensitivity C_0 results in $F[\rho](k_x, k_y)$ as shown in Eq. (1). The application of the sinusoidal sensitivity $C_{\Delta k}$ is described by combining Eqs. (1) and (3)

$$\begin{aligned} S(k_x, k_y) &= \iint dx dy \rho(x, y) \exp(-ik_x x - ik_y y + i\Delta k_y y) \\ &= F[\rho](k_x, k_y - \Delta k_y) \end{aligned} \quad (5)$$

i.e., the signal is shifted by $-\Delta k_y$ in k_y direction. Hence, by modifying the value Δk_y , appropriately, this result can be used to calculate a posteriori all not originally acquired k-space lines as a superposition of data $S^j(k_x, k_y)$ of the single coil elements indexed by j

$$S(k_x, k_y - \Delta k_y) = \sum_j n_{\Delta k}^j S^j(k_x, k_y). \quad (6)$$

Newer techniques like AUTO-SMASH or GRAPPA use a similar approach for completing the k-space as described above, however, instead of a separate calibration

scan the coil sensitivities are determined by some additional phase-encoded lines in k-space [4, 5]. If the single line $S^j(k_x, k_y - \Delta k_y)$ is measured as additional auto-calibration signal, the coefficients $n_{\Delta k}^j$ can be calculated by comparing this line with its also known neighboring line $S^j(k_x, k_y)$

$$\begin{aligned} S(k_x, k_y - \Delta k_y) &= \sum_j n_0^j S^j(k_x, k_y - \Delta k_y) \\ &= \sum_j n_{\Delta k}^j S^j(k_x, k_y). \end{aligned} \quad (7)$$

One can assume that the coefficients n_0^j are approximately 1, i.e., the unweighted sum of the profiles of the coil elements yield a sufficiently homogeneous signal distribution. Thus, the coefficients $n_{\Delta k}^j$ can be determined as the solution of a system of linear equations that are obtained from Eq. (7) for the different values of k_x .

Reconstruction in the image domain

In SENSE MRI and related techniques, images with reduced k-space sampling density are first conventionally reconstructed for each receiver coil element and then those individual images with folding artifacts are processed to yield an artifact-free final image [6].

The image intensity $I^j(x, y)$ of the j -th receiver coil element depends on the product of the coil sensitivity $C^j(x, y)$ and the original proton density $\rho(x, y)$, but also on the superimposed image intensities due to folding $C^j(x, y+n\Delta y) \rho(x, y+n\Delta y)$:

$$\begin{aligned} I^j(x, y) &= C^j(x, y) \rho(x, y) + C^j(x, y+\Delta y) \rho(x, y+\Delta y) \\ &+ C^j(x, y+2\Delta y) \rho(x, y+2\Delta y) + \dots \end{aligned} \quad (8)$$

The number of summands $C^j(x, y+n\Delta y) \rho(x, y+n\Delta y)$ depends on the size of the reduced field of view which again is determined by the acceleration factor R ; the aliasing distance Δy is given by full FOV in y direction divided by R . The influence of noise is not described by this equation but can be taken into account as receiver noise matrix [6]. For a coil array with L elements, L different equations analogous to Eq. (8) can be obtained that can be summarized in a vector equation

$$\mathbf{I} = \mathbf{C} \cdot \boldsymbol{\rho} \quad (9)$$

with a $1 \times L$ vector \mathbf{I} , an $R \times L$ matrix \mathbf{C} and a $1 \times R$ vector $\boldsymbol{\rho}$. To calculate the original proton density $\boldsymbol{\rho}$ from the images I^j , this system of equations must be solved by inverting Eq. (9): $\boldsymbol{\rho} = \mathbf{C}^{-1} \mathbf{I}$. This is possible, if $L > R$ and if the coil

sensitivity profiles are sufficiently distinct. As in the SMASH approach, the coil sensitivities must be known before image reconstruction; they can be measured during a pre-scan or, e.g., in mSENSE (modified SENSE) as extra lines during the image acquisition. Since the sensitivity profiles can be assumed to vary only slowly in space, the acquisition of low resolution sensitivity maps is sufficient for image reconstruction. Thus, only a comparably small number of extra lines need to be added to the PAT scan, and the acquisition time is not considerably increased.

Having acquired such a dataset with a certain number of reference lines, both the AUTO-SMASH/GRAPPA and the mSENSE method can be used to reconstruct the final image. It depends on the application which of these techniques yields the better results, e.g., they have different noise characteristics and SENSE-related methods are more sensitive to folding artifacts in the *un-folded* (full-FOV) image. Due to the fact, that SENSE techniques are not able to unfold *pre-folded* images without pronounced artifacts (folding artifacts are propagated toward the image center), they are less suitable for applications like e.g. cardiac imaging or angiography (Fig.12, 13).

Noise in PAT

In general, the trade-off for reducing the number of acquired k-space lines is a decreased signal-to-noise ratio (SNR) [6]. As in conventional imaging, reducing the FOV by a factor R at constant voxel size decreases the SNR by $1/\sqrt{R}$. However, the SNR of PAT images is generally further reduced by the so-called geometry factor g . This factor, which depends on the position in the final image, describes the ability of the chosen coil configuration to separate image intensities in a pixel into the different superimposed contributions; the geometry factor g is 1 in the case of ideal coil geometries but typically greater than 1. Thus, the resulting SNR of PAT images is

$$\text{SNR}_{\text{PAT}} = \text{SNR}_{\text{full}} / (g \sqrt{R}) \quad (9)$$

Due to this loss of SNR, parallel acquisition techniques are especially useful when the corresponding conventional image has a high SNR like in contrast-enhanced angiography or in techniques that are rather restricted by acquisition time as in breath-hold examinations than by SNR considerations.

An exception to the reduction of SNR is observed when PAT is combined with single-shot imaging techniques like EPI (echo-planar imaging) or HASTE (half-Fourier acquired single-shot turbo spin echo). In this case, the loss of SNR can be considerably reduced, and under certain conditions the SNR might even increase. This can

be explained by considering the signal decay due to the transversal T2 or T2* relaxation in tissue. Signal intensities of the acquired echoes decrease exponentially during the HASTE or EPI read-out because of these relaxation effects. Thus, the last echoes of long echo trains have comparably low signal intensities reducing the over-all SNR of the resulting image and leading to a blurring effect. By applying PAT, the length of the echo trains and hence the transversal relaxation effect can be reduced which results in an increase of SNR.

Materials and Methods

The iPAT applications described in the following sections were performed on a 1.5 T whole-body MR system (Magnetom Sonata; Siemens Medical Solutions; Erlangen, Germany). This system provides 8 parallel receive channels for parallel imaging and is equipped with a gradient subsystem with maximum gradient strength of 40 mT/m and maximum slew rate of 200 mT/m/ms. For signal reception, either a 12-element surface-coil array or, alternatively, a combination of flexible body surface coils and the spine coil array was used. The dedicated 12-element iPAT coil consists of 2×6 elements located anterior and posterior of the patient. When selecting all coil elements, 8 of the 12 elements are combined in pairs of 2 to reduce the number of output channels to 8 corresponding to the 8 RF receive channels of the MR system.

With the latest Numaris 4 software release (Syngo MR2002B; Siemens Medical Solutions; Erlangen, Germany), iPAT functionality is provided for a number of different MR pulse sequences, allowing to select either a GRAPPA or an mSENSE reconstruction algorithm with acceleration factors between 2 and 4.

Cardiac Functional Imaging

Cardiac magnetic resonance imaging has been established as the standard of reference in assessment of global and regional myocardial function because of its high accuracy as well as its high reproducibility [10, 11]. Cardiac function is most commonly assessed based on a stack of double oblique short axis slices using segmented fast low angle shot (FLASH) or steady-state free precession (SSFP) techniques like TrueFISP sequences acquiring a single slice cine-loop within single breath-holds. Recently developed real-time imaging techniques using SSFP sequences also allow for a single breath-hold multi-slice evaluation of global cardiac function [11, 12]. However, these techniques provide only limited temporal resolution (70–90 ms) affecting volumetric results. Imaging algorithms using PAT allow for further improvements of temporal resolution. In a recent study in 5 healthy volunteers and 4

patients, results of a real-time single breath-hold TrueFISP sequence using iPAT have been compared with state-of-the-art non-PAT segmented TrueFISP techniques.

For the iPAT-supported real-time technique, the GRAPPA reconstruction algorithm has been chosen. The acceleration factor was set to 2 and the number of reference lines to 12. Details of the spatial resolution can be seen in (Table 1). Compared to a comparable non-PAT technique the temporal resolution can be improved from 71 ms to 48 ms. The segmented TrueFISP technique allowed a temporal resolution of 42 ms (Table 1). All techniques used echo-sharing. Left ventricular volumetry for calculating end-diastolic volume (EDV), end-systolic volume (ESV), and ejection fraction (EF) has been performed using identical slice positions. Coverage of the left ventricle was provided with 9–11 slices with a slice distance of 10 mm. Acquired data sets were evaluated using commercially available semiautomatic segmentation algorithms (ARGUS; Siemens Medical Solutions; Erlangen, Germany).

Table 1. Sequence parameters for functional cardiac SSFP MRI

Parameter	Segmented TrueFISP	Real-time iPAT TrueFISP ⁺
Temporal resolution (ms)	42	48
TE (ms)	1.5	0.9
Matrix (read × phase)	256×256	128×60
Field of view (mm ²)	380×285	400×250
Pixel size (mm ²)	1.5×1.5	3.1×4.2
Slice thickness (mm)	8	8

⁺ using Grappa factor 2; 12 reference lines

Results of real-time TrueFISP imaging showed excellent correlation to those of segmented TrueFISP imaging for EDV ($r=.93$; $P<.001$) and ESV ($r=.99$; $P<.001$) volumes as well as for EF ($r=.99$; $P<.001$) (Table 2). Values of EDV did not show significant differences between segmented TrueFISP (158.7 ± 46.8 ml) and real-time TrueFISP (150.6 ± 44.8 ml) ($P=.21$). Also for ESV real-time TrueFISP (79.9 ± 43.2 ml) did not lead to significant differences compared to segmented TrueFISP (82.5 ± 45.9 ml) ($P=.25$). Exact results for EF were 50.1 ± 13.1 ml and 49.4 ± 12.1 ml for real-time TrueFISP and segmented TrueFISP, respectively ($P=.49$) (Table 2). However, the reduced spatial resolution leads to blurring of the blood-myocardial border which complicated automated edge detection.

Table 2. Results of single breath-hold multi-slice real-time SSFP and segmented single-slice TrueFISP in assessment of LV volumes

Volumetric Parameter	Real-time TrueFISP (iPAT)	Segmented TrueFISP	P	R
EDV (ml)	150.6±44.8	158.7±46.8	0.21	0.93
ESV (ml)	79.9±43.3	82.5±45.9	0.25	0.99
EF (%)	50.1±13.1	49.4±12.1	0.49	0.99

R=Pearson's correlation coefficient

These preliminary results show that the improvement in temporal resolution based on PAT leads to accurate evaluation of global functional parameters (Fig. 3, 4). This demonstrates a marked improvement compared to recent studies without parallel imaging algorithms [11]. However, the reliability of these real-time techniques in assessment of regional myocardial analysis has to be proven.

Parallel k-space sampling algorithms are still prone to wrap-around artifacts. In double oblique short-axis cardiac MRI, image quality can be dramatically improved by rotating the FOV; thus, artifacts are moved from the ventricle to less important peripheral image regions (Fig. 5).

The current study used an acceleration factor of 2. Higher speed-up factors ($R=3$, $R=4$) further improve temporal resolution but also lead to pronounced artifacts (Fig. 6). Increasing the number of reference lines will again reduce artifacts but also reduces temporal resolution.

Besides real-time SSFP imaging also segmented SSFP imaging can be accelerated using PAT. In addition, further studies have to be performed about the use of PAT in myocardial perfusion imaging. The speed-up of myocardial perfusion techniques might improve spatial resolution or increase the number of slices acquired each heartbeat.

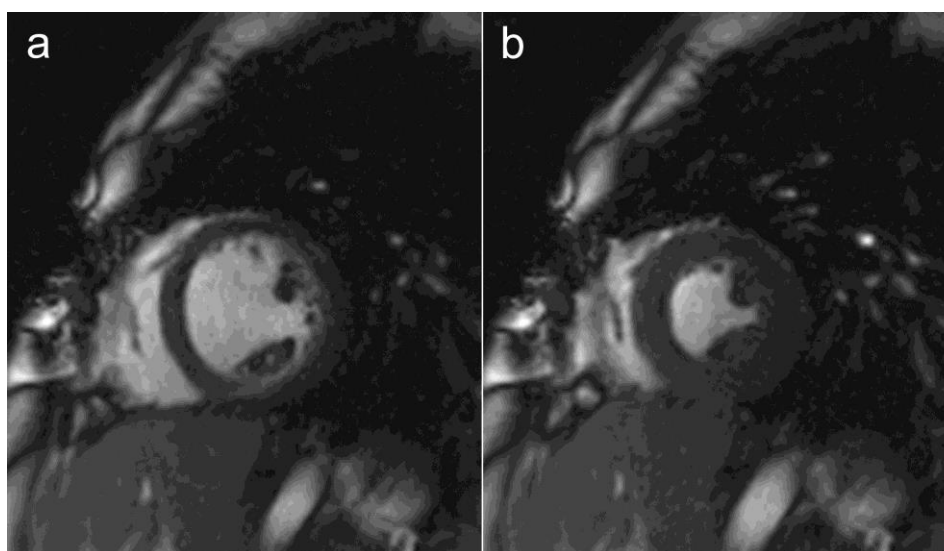


Figure 3. Segmented TrueFISP: Midventricular end-diastolic (a) and end-systolic (b) short axis views in a patient with dilated cardiomyopathy (DCM) and marked reduction of ejection fraction.

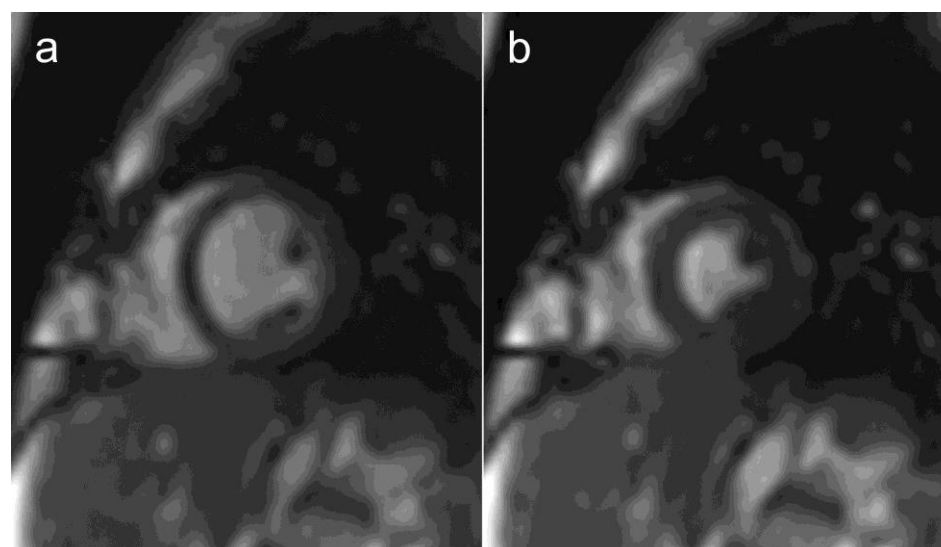


Figure 4. Real-time TrueFISP with iPAT: Corresponding views to (Fig. 3). End-diastolic (a) and end-systolic (b) short axis views in the same patient with DCM. Note the artifact within the left ventricle.

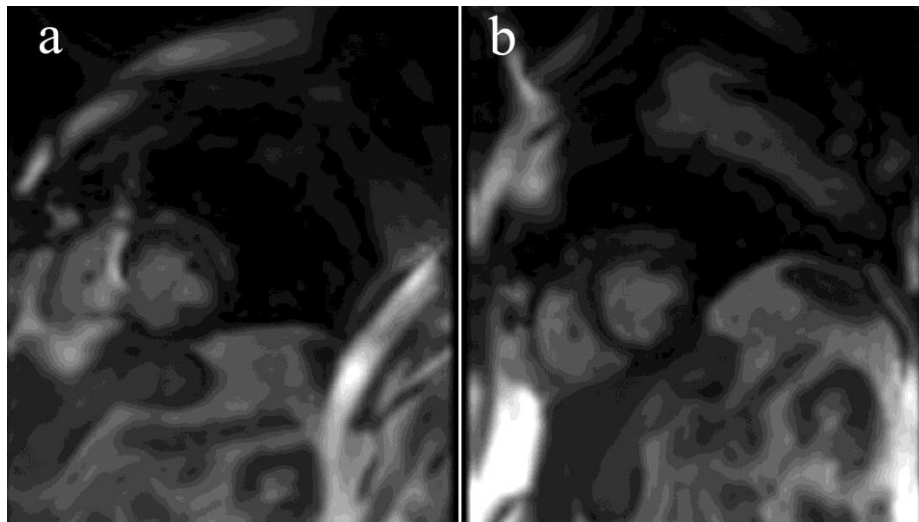


Figure 5. Real-time TrueFISP with iPAT (GRAPPA algorithm): comparison of image acquisition with standard orientation (a) and rotated FOV (b). Note the reduction of artifacts due to the rotated FOV.

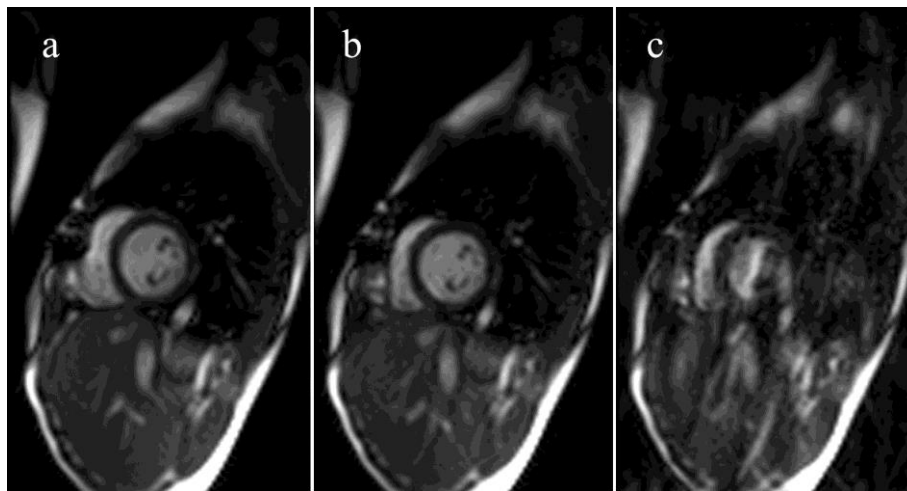


Figure 6. Real-time TrueFISP with iPAT (GRAPPA algorithm): comparison of image acquisition with iPAT acceleration factors of 2, 3, and 4 (a, b, and c, respectively).

Morphologic and functional imaging of patients with pulmonary hypertension

The purpose of this study was to assess the use of 3D contrast-enhanced MR angiography (MRA) and MR perfusion imaging in combination with iPAT for the differentiation of patients with primary and secondary pulmonary arterial hypertension (PAH). So far, experiences on MR perfusion imaging of the lung are still limited and various approaches are being used. Amundsen et al. have used a conventional FLASH technique to demonstrate perfusion defects in patients with pulmonary embolism and in patients with chronic obstructive pulmonary disease (COPD) [13, 14]. Other approaches have been tried using a HASTE sequence [15] or flow-sensitive inversion recovery techniques [16]. Yet, parallel imaging techniques imply the great advantage of a significant increase in temporal and spatial resolution.

26 patients with known or suspected PAH were examined with the 1.5 T MR system described above, 13 with iPAT sequences and 13 with conventional non-PAT sequences. Using GRAPPA with the dedicated 12-element iPAT coil, a temporal resolution of 1.2 seconds per phase was possible for dynamic perfusion imaging, acquiring 25 dynamic phases in 30 seconds. High resolution angiograms were acquired with a 512 matrix ($0.7 \times 1.0 \times 1.5 \text{ mm}^3$ voxel size) in 20 seconds breath-hold time. For both dynamic perfusion and high-resolution angiography, an iPAT acceleration factor of 2 was used. MR angiography as well as perfusion imaging was performed using a three-dimensional gradient-echo FLASH sequence with slice-selective pulses. (Table 3) shows a comparison of imaging parameters using the non-PAT and the iPAT sequences. The reformatted 3D MRA images and the dynamic perfusion images were analyzed for caliber irregularities, segmental perfusion defects, and intravascular thrombi. Perfusion parameters were assessed qualitatively (signal intensi-

ty versus time curves) as well as quantitatively. Results were compared to digital pulmonary angiography, perfusion scintigraphy, and clinical course of the patient.

Results of this study are shown in (Fig. 7–10). Using the parallel acquisition technique, excellent visualization of subsegmental vessels was possible in the angiographic images in all cases. Time-resolved perfusion images allowed a reliable detection of small segmental and subsegmental perfusion defects. The combination of both morphological and functional MR imaging highly agreed with the results of pulmonary angiography and scintigraphy, as well as final clinical diagnosis. Additionally, MRI provided information about morphological right heart changes

caused by chronic pulmonary hypertension. Using non-PAT methods, visualization of perfusion defects and intravascular thrombi is possible, as shown in (Fig. 9) and (Fig. 10), although with lower temporal and spatial resolution than using iPAT methods.

In conclusion, we could substantially improve the temporal resolution as well as the spatial resolution by using iPAT. The combination of morphological and functional MR imaging enables the differentiation of patients with primary and secondary pulmonary arterial hypertension with a comparable diagnostic accuracy as pulmonary angiography and perfusion scintigraphy.

Table 3. Comparison of imaging parameters for high-resolution magnetic resonance pulmonary angiography and perfusion imaging using a non-iPAT and an iPAT technique

	Angiography		Perfusion		
	Non-PAT	iPAT	Non-PAT	iPAT	
TR (ms)	3.3	2.9	1.7	1.7	
TE (ms)	1.2	1.2	0.7	0.6	
Matrix (read × phase)	512×256	512×352	256×128	256×128	
Field of view (mm ²)	380×342	380×342	380×342	380×342	
Pixel size (mm ²)	0.7×1.3	0.7×1.0	1.5×2.7	1.5×2.7	
Slice thickness (mm)	2.0	1.5	5.0	4.0	
# slices	64	88	16	24	
# phases	—	—	24	25	
Acquisition time / phase (s)	—	—	1.1	1.2	
Total acquisition time (s)	21	22	27	30	

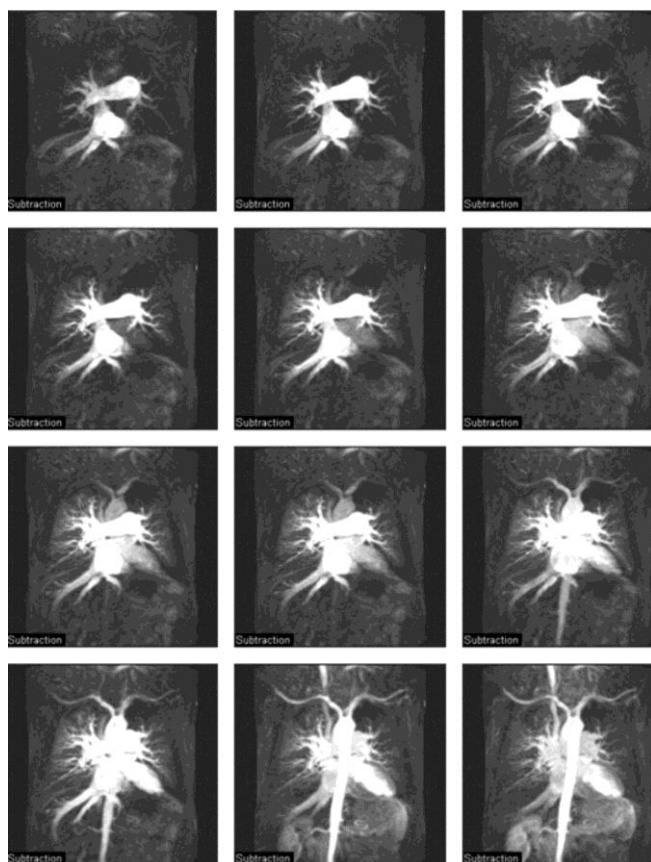


Figure 7. Dynamic pulmonary perfusion imaging using the iPAT technique, acquiring a slab of 24 images each 1.2 seconds. Perfusion defects are shown in the left upper lobe and right lower lobe.



Figure 8. Example of an iPAT high-resolution magnetic resonance pulmonary angiography of the same patient as in (Fig. 7). A significant reduction of arterial enhancement can be demonstrated in the left upper lobe and right lower lobe due to central thromboembolic occlusions.

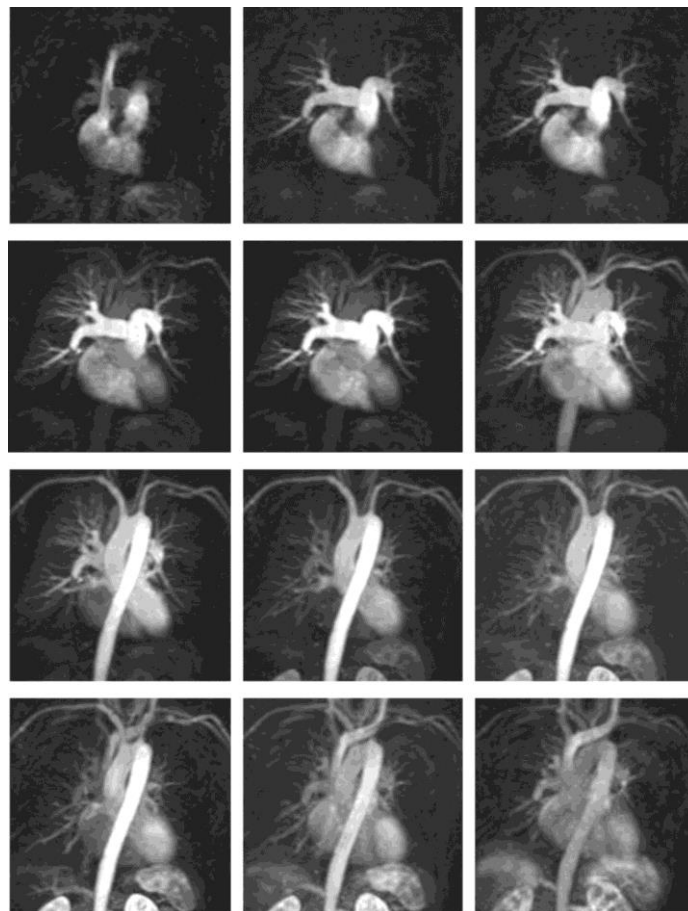


Figure 9. Example of a perfusion study using a conventional non-PAT sequence. Perfusion defects are shown in the left middle and lower lobe and in the right middle lobe.



Figure 10. Example of a conventional non-PAT high-resolution magnetic resonance pulmonary angiography of the same patient as in (Fig. 9). A significant reduction of arterial enhancement can be demonstrated in the right middle lobe and left middle and lower lobe due to thromboembolic occlusions.

High-resolution MR angiography of the renal arteries

Since its introduction by Prince et al. 3D gadolinium-enhanced magnetic resonance angiography (3D-Gd-MRA) has gained high popularity as a non-invasive imaging alternative for grading of renal artery stenosis [17]. High accuracies of over 90% have been reported by numerous researchers in the past five years [18]. Nevertheless, 3D-Gd-MRA is still notoriously known for overgrading high-grade renal artery stenoses and missing low-grade lesions, thereby limiting its overall clinical acceptance. The recent Dutch RADISH multicenter trial presented less encouraging results with overall accuracies of only 85% compared to DSA. In addition, no reliable data on grading of stenoses of the more distal main renal artery or segmental arteries exists, yet [19].

One major limiting factor is spatial resolution. For standard breath-hold acquisitions with bolus administration of extracellular, non-intravascular gadolinium chelates, the maximum achievable spatial resolution represents a compromise between scan time, anatomic coverage and SNR. Current imaging protocols usually obtain images with a maximum of 1.5 mm^3 isotropic resolution which still represents 5 to 7 fold less than that of digital subtraction angiography (DSA). In a renal artery with a diameter of 7–8 mm, an isotropic voxel size of at least 1 mm^3 is

required for accurate depiction of a 90% reduction in lumen diameter.

Based on previous calculations, it is expected that voxel sizes of less than 1 mm^3 are substantially limited by SNR constraints [20]. Therefore, it was our aim to increase spatial resolution to maximum values within this range. The iPAT strategy was used in combination with a fast 3D FLASH sequence (TR = 3.79 ms, TE = 1.3 ms, Bandwidth = 350 Hz/pixel, flip angle = 25°). A spatial resolution of $0.9 \times 0.8 \times 1 \text{ mm}^3$ was achieved within an acquisition time of 23 seconds. For signal receiving, a combination of flexible body surface coils and the spine coil array was used with a total of six array elements. For data acquisition and reconstruction, both the SENSE and GRAPPA algorithms were used and compared in terms of artifacts. A PAT acceleration factor of 2 was used for all scans.

Measurements were first tested in a tubing phantom with different degrees of stenoses down to a lumen diameter of 1 mm. In addition, more than 30 patients were imaged with the above protocol. Contrast media (Gadobutrol, Schering AG, Germany) was administered at a dose of 1.25 mmol/kg body weight with an injection rate of 2 ml/s.

In the phantom, the higher resolution of the iPAT scans resulted in a substantially better definition of the residual 1 mm lumen of the high-grade stenosis compared to a standard acquisition without iPAT and a spatial resolution of $1.3 \times 0.8 \times 1.3 \text{ mm}^3$ (Fig. 11). These results could be re-

produced in the patients with renal artery stenosis. In cases with high-grade stenoses of 90%, the remaining vessel lumen was still clearly defined, even on the maximum intensity projections (MIP). For stenoses greater than 90%, the remaining lumen was still seen on an individual slice of the source data but then disappeared on the MIP images.

In the iPAT images, SNR decreased by a factor of about 1.5 compared to the data without iPAT. This decrease could be visually noticed in the source images, however, the intravascular signal was still acceptable. In the MIP images, the overall decrease in SNR was hardly detected.

One limitation of the PAT approach is the propagation of aliasing artifacts into the center of the image. These artifacts could be theoretically avoided by extending the FOV in the left-to-right direction so that no aliasing occurs

at all. In clinical practice however, this would mean a substantial increase in scan time, in particular in large patients. In addition, not all patients are able to put their arms over the head. Therefore some degree of aliasing into the margins of the FOV has to be accepted. The propagated artifacts usually were only mild and therefore did not limit the accurate assessment of fine vessel details. In addition, they were less prominent when an AUTO-SMASH like algorithm such as GRAPPA instead of the SENSE technique was used (Fig. 12, 13).

In conclusion, high-resolution contrast-enhanced MR angiograms of the renal arteries are possible using the parallel acquisition techniques with improved definition of small vessel lumen. Limitations due to SNR and artifacts have to be considered but do not substantially affect the overall diagnostic value of technique.

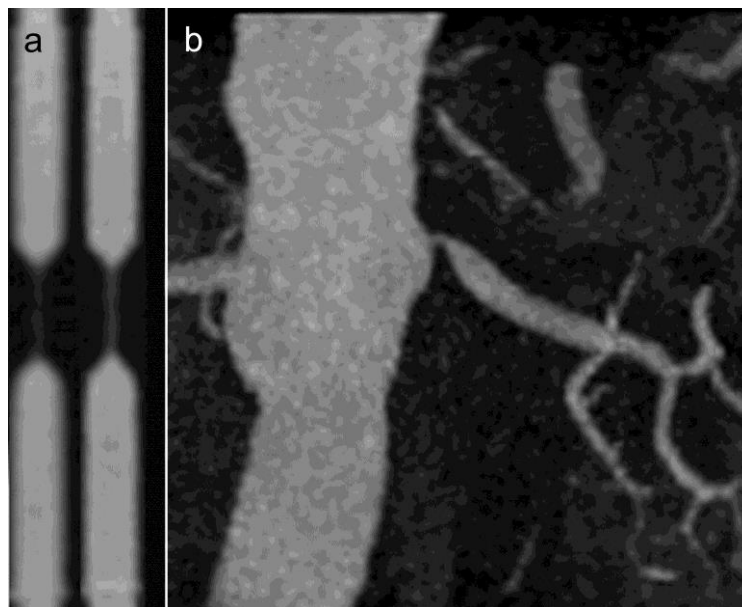


Figure 11. (a) Comparison of 3D FLASH sequences in a stenosis phantom without (left) and with (right) integrated parallel acquisition techniques (GRAPPA). Voxel size was 1.4 mm^3 versus 0.7 mm^3 , respectively. Note that for the iPAT sequence the 1 mm lumen of the stenosis is much better defined. (b) Application of iPAT in a patient with left renal artery stenosis. Despite the high-grade stenosis, the residual lumen is well seen on this MIP image.

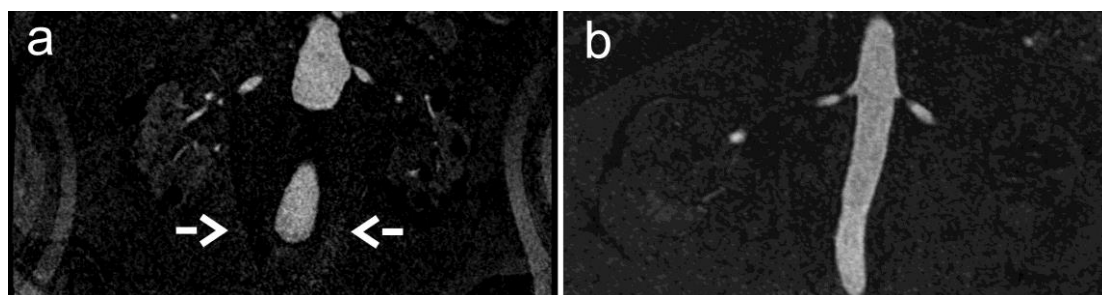


Figure 12. Source data from 3D-Gd-MR angiograms of different patients using the SENSE (a) and GRAPPA (b) algorithm. Despite some appreciated background noise intravascular signal is adequate in both images. In the SENSE images a marked ellipsoid artifact is seen in the center of the image arising from propagated aliased signal from the margin of the FOV (arrows). In the GRAPPA image, this artifact is substantially reduced and hardly noticed.

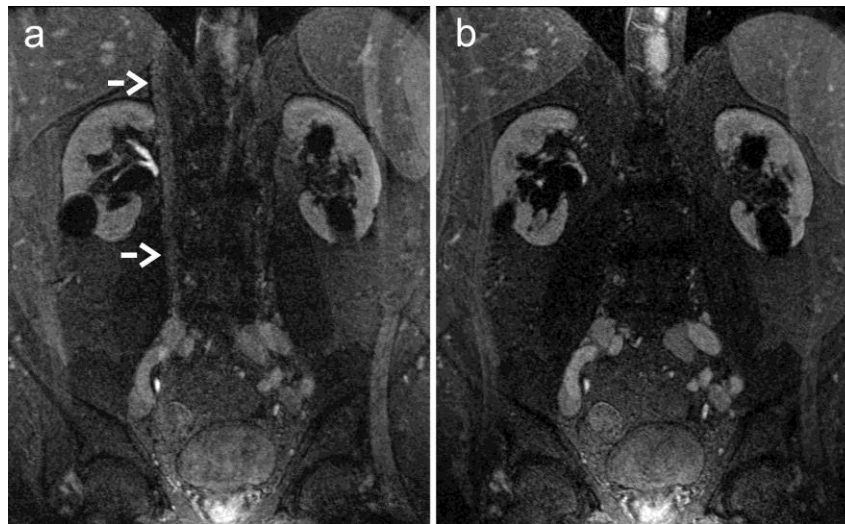


Figure 13. Comparison of propagated aliasing artifacts in the same patient using the SENSE (a) and GRAPPA (b) algorithm. The field of view was on purpose set to only 32 cm to enforce aliasing of the arms. In the SENSE images severe artifacts occur in the center of the image (arrows) while these artifacts are virtually absent on the GRAPPA images.

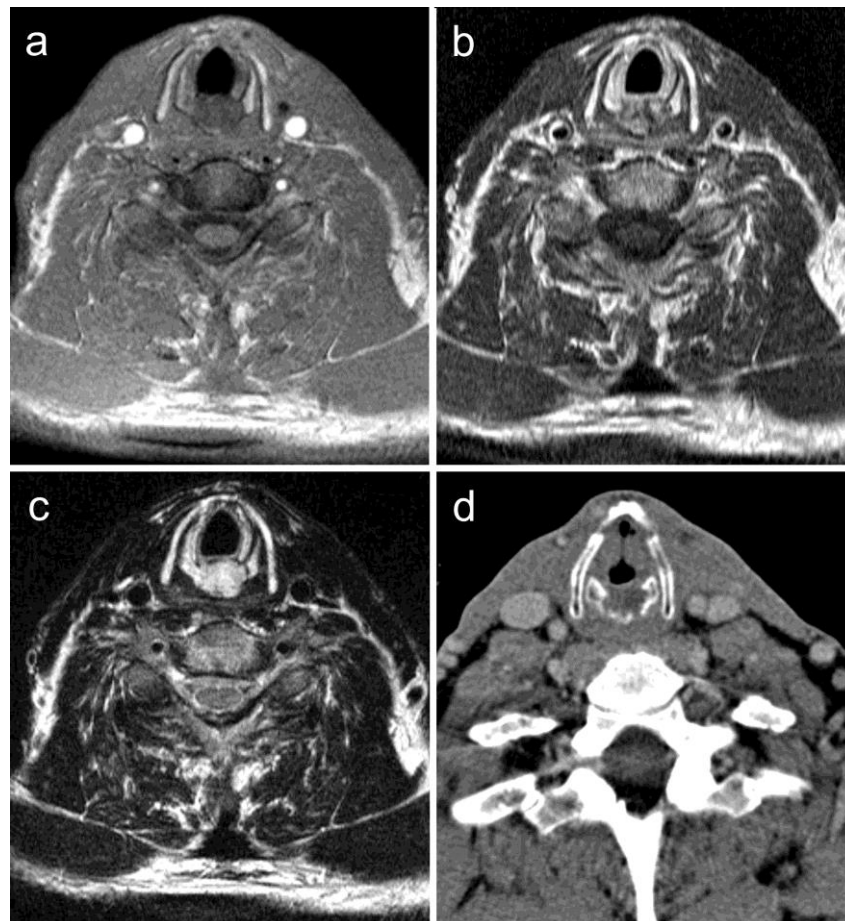


Figure 14. Axial high-resolution MRI scan through the subglottic larynx, all images show the same scan position. Images demonstrate large subglottic tumor infiltrating the cricoid cartilage. (a) T1-weighted axial image showing almost muscle-isointense tumor. (b) T1-weighted axial image demonstrating inhomogeneous contrast-enhancement of the tumor. (c) T2-weighted axial image showing hyperintense tumor-tissue. (d) CT scan demonstrating destruction of cricoid cartilage by not significantly enhancing tumor mass. Chondroma was found at surgery.

Larynx MRI with parallel acquisition technique – a novel approach to MRI of organs in movement

Imaging examination of the larynx with MRI is difficult due to respiration and/or swallowing [21–24]. These limitations result in excessive motion artifacts using conventional MR sequences. As moving organs can be more clearly visualized by reducing the image acquisition time, we used iPAT to accelerate the acquisition. With this approach, the number of acquisitions can be increased without changing the total examination time, and the same image resolution and a comparable SNR as in a conventional scan can be achieved.

In a recent study, we examined 10 consecutive patients suffering from suspected laryngeal carcinoma using the 1.5 T MR system and the dedicated 12-element iPAT coil array described above. We acquired T1-weighted and T2-weighted images; the scan parameters are given in (Table 4). For image reconstruction we used the GRAPPA algorithm with an acceleration factor of 2. Two observers individually evaluated the different sequences concerning the image quality and tumor extent.

The acquired images with GRAPPA reconstruction showed less motion and pulsation artifacts than conventional MR images; examples are shown in (Fig. 14). Moreover the used iPAT sequences lead to better delineation of tumor extent than non-PAT MRI sequences, thus allowing accurate diagnosis of laryngeal carcinoma. This is particularly important for an accurate assessment of tumor infiltration of the surrounding fat plane of the contralateral vocal cord which directly influences the surgical approach.

Table 4. Sequence parameters for laryngeal imaging with iPAT

	T1-w GRE	T2-w TSE
TR (ms)	155	3970
TE (ms)	4.48	89
Matrix (read × phase)	512×384	512×384
Field of view (mm ²)	300×281.3	300×281.3
Pixel size (mm ²)	0.6×0.7	0.6×0.7
Slice thickness (mm)	3.5	3.5
# acquisitions	5	3
iPAT acceleration factor	2	2
Total acquisition time (s)	38	57

Conclusion

Parallel acquisition methods can be implemented for many different MRI sequences. Although these methods generally decrease the SNR, they also provide different important advantages depending on the specific application. The iPAT applications presented in this article demonstrate some of these advantages.

In functional cardiac imaging, the reduction of acquisition time was used to improve the *temporal* resolution of a real-time TrueFISP sequence; thereby, a temporal resolution of less than 50 ms could be achieved using iPAT compared with more than 70 ms in the corresponding non-PAT sequence. In both pulmonary and renal MRA as well as in lung perfusion imaging, iPAT was applied to increase the *spatial* resolution of FLASH sequences within breath-hold time. All these different applications have in common that they are performed during breath-hold and thus are limited rather by the acquisition time than by SNR considerations. Hence, they are especially suited for iPAT methods.

Motion sensitivity of high-resolution larynx MRI could be considerably reduced by averaging a number of shorter acquisitions instead of acquiring data in a single longer scan. By spending the same total acquisition time as in conventional sequences, there is no significant SNR loss; however, the amount of motion during a single acquisition is reduced.

For the presented applications, the GRAPPA reconstruction algorithm was favored because the obtained image quality was equal or better compared to the mSENSE reconstruction. In particular the ability of the GRAPPA technique to handle small FOVs with folding artifacts recommends it for cardiac imaging and angiography.

Many other applications are expected to benefit from iPAT as well, like e.g. single-shot RARE or HASTE imaging of the abdomen or echo-planar imaging of the brain. Future studies are required to establish examination protocols with optimized iPAT sequences for these different applications.

References

1. Bammer R, Keeling SL, Augustin M, Pruessmann KP, Wolf R, Stollberger R, Hartung HP, Fazekas F. Improved diffusion-weighted single-shot echo-planar imaging (EPI) in stroke using sensitivity encoding (SENSE). *Magn Reson Med*. 2001; 46: 548–554.
2. Bydder M, Larkman DJ, Hajnal JV. Detection and elimination of motion artifacts by regeneration of k-space. *Magn Reson Med*. 2002; 47: 677–686.
3. Sodickson DK, Manning WJ. Simultaneous acquisition of spatial harmonics (SMASH): fast imaging with radiofrequency coil arrays. *Magn Reson Med*. 1997; 38: 591–603.
4. Jakob PM, Griswold MA, Edelman RR, Sodickson DK. AUTO-SMASH: a self-calibrating technique for SMASH imaging. *MAGMA*. 1998; 7:42–54.
5. Griswold MA, Jakob PM, Heidemann RM, Nittka M, Jellus V, Wang J, Kiefer B, Haase A. Generalized autocalibrating partially parallel acquisitions (GRAPPA). *Magn Reson Med*. 2002; 47: 1202–1210.
6. Pruessmann KP, Weiger M, Scheidegger MB, Boesiger P. SENSE: sensitivity encoding for fast MRI. *Magn Reson Med*. 1999; 42: 952–962.
7. Griswold MA, Jakob PM, Nittka M, Goldfarb JW, Haase A. Partially parallel imaging with localized sensitivities (PILS). *Magn Reson Med*. 2000; 44: 602–609.
8. Kyriakos WE, Panych LP, Kacher DF, Westin CF, Bao SM, Mulkern RV, Jolesz FA. Sensitivity profiles from an array of coils for encoding and reconstruction in parallel (SPACE RIP). *Magn Reson Med*. 2000; 44: 301–308.
9. Semelka RC, Tomei E, Wagner S, Mayo J, Kondo C, Suzuki J, Caputo GR, Higgins CB. Normal left ventricular dimensions and function: interstudy reproducibility of measurements with cine MR imaging. *Radiology*. 1990; 174: 763–768.
10. Pattynama PM, Lamb HJ, van der Velde EA, van der Wall EE, de Roos A. Left ventricular measurements with cine and spin-echo MR imaging: a study of reproducibility with variance component analysis. *Radiology*. 1993; 187: 261–268.
11. Barkhausen J, Goyen M, Ruhm SG, Eggebrecht H, Debatin JF, Ladd ME. Assessment of ventricular function with single breath-hold real-time steady-state free precession cine MR imaging. *AJR Am J Roentgenol*. 2002; 178: 731–735.
12. Lee VS, Resnick D, Bundy JM, Simonetti OP, Lee P, Weinreb JC. Cardiac function: MR evaluation in one breath hold with real-time true fast imaging with steady-state precession. *Radiology*. 2002; 222: 835–842.
13. Amundsen T, Torheim G, Waage A, Bjermer L, Steen PA, Haraldseth O. Perfusion magnetic resonance imaging of the lung: characterization of pneumonia and chronic obstructive pulmonary disease. A feasibility study. *J Magn Reson Imaging*. 2000; 12: 224–231.
14. Amundsen T, Torheim G, Kvistad KA, Waage A, Bjermer L, Nordlid KK, Johnsen H, Asberg A, Haraldseth O. Perfusion abnormalities in pulmonary embolism studied with perfusion MRI and ventilation-perfusion scintigraphy: an intra-modality and inter-modality agreement study. *J Magn Reson Imaging*. 2002; 15: 386–394.
15. Hatabu H, Tadamura E, Prasad PV, Chen Q, Buxton R, Edelman RR. Noninvasive pulmonary perfusion imaging by STAR-HASTE sequence. *Magn Reson Med*. 2000; 44: 808–812.
16. Mai VM, Hagspiel KD, Christopher JM, Do HM, Altes T, Knight-Scott J, Stith AL, Maier T, Berr SS. Perfusion imaging of the human lung using flow-sensitive alternating inversion recovery with an extra radiofrequency pulse (FAIRER). *Magn Reson Imaging*. 1999; 17: 355–361.
17. Prince MR, Narasimham DL, Stanley JC, Chenevert TL, Williams DM, Marx MV, Cho KJ. Breath-hold gadolinium-enhanced MR angiography of the abdominal aorta and its major branches. *Radiology* 1995; 197: 785–792.
18. Dong Q, Schoenberg SO, Carlos RC, Neimatallah M, Cho KJ, Williams DM, Kazanjian SN, Prince MR. Diagnosis of renal vascular disease. *Radiographics* 1999; 19: 1535–1554.
19. Schoenberg SO, Bock M, Knopp, MV, Essig M, Laub G, Hawighorst, H, Zuna I, Kallinowski F, van Kaick G. Renal arteries: Optimization of 3D Gadolinium MR Angiography with bolus-timing independent fast multiphase acquisition in a single breath hold. *Radiology* 1999; 201: 667–676.
20. Heid O: The outer limits of contrast enhanced MR angio (gradient performance, resolution, speed, etc) [Abstract]. In: Proceedings of the tenth international workshop on magnetic resonance angiography, Park City, Utah, The International MR Angio Club 1998: 75.
21. Curtin HD. Imaging of the larynx: current concepts. *Radiology*. 1989; 173: 1–11.
22. Mukherji SK, Pillsbury HR, Castillo M. Imaging squamous cell carcinomas of the upper aerodigestive tract: what clinicians need to know. *Radiology*. 1997; 205: 629–646.
23. Hermanns R. Imaging of the Larynx. 2001; Springer, Berlin Heidelberg New York.
24. Keberl M, Kenn W, Hahn D. Current concepts in imaging of laryngeal and hypopharyngeal cancer. *Eur Radiol*. 2002; 12:1672–1683.